Quantification of β-Amyloidosis and rCBF with Dedicated PET, 7 T MR Imaging, and High-Resolution Microscopic MR Imaging at 16.4 T in APP23 Mice

Florian C. Maier[1], Marianne D. Keller[2,3], Daniel Bukala[1], Benjamin Bender[4], Julia G. Mannheim[1], Ian M. Brereton[2], Graham J. Galloway[2], and Bernd J. Pichler[1]

[1]Werner Siemens Imaging Center, Department of Preclinical Imaging and Radiopharmacy, Eberhard Karls University Tübingen, Tübingen, Germany; [2]University of Queensland, Centre for Advanced Imaging, Brisbane, Australia; [3]South Australian Health and Medical Research Institute, Adelaide, Australia; and [4]Department for Neuroradiology, University Hospital Tübingen, Tübingen, Germany

We present a combined PET/7 T MR imaging and 16.4 T microscopic MR imaging dual-modality imaging approach enabling quantification of the amyloid load at high sensitivity and high resolution, and of regional cerebral blood flow (rCBF) in the brain of transgenic APP23 mice. Moreover, we demonstrate a novel, voxel-based correlative data analysis method for in-depth evaluation of amyloid PET and rCBF data. **Methods:** We injected ^{11}C-Pittsburgh compound B (PIB) intravenously in transgenic and control APP23 mice and performed dynamic PET measurements. rCBF data were recorded with a flow-sensitive alternating inversion recovery approach at 7 T. Subsequently, the animals were sacrificed and their brains harvested for ex vivo microscopic MR imaging at 16.4 T with a T_2*-weighted gradient-echo sequence at 30-μm spatial resolution. Additionally, correlative amyloid histology was performed. The ^{11}C-PIB PET data were quantified to nondisplaceable binding potentials (BP_{ND}) using the Logan graphical analysis; flow-sensitive alternating inversion recovery data were quantified with a simplified version of the Bloch equation. **Results:** Amyloid load assessed by both ^{11}C-PIB PET and amyloid histology was highest in the frontal cortex of transgenic mice (^{11}C-PIB BP_{ND}: 0.93 ± 0.08; amyloid histology: 15.1% ± 1.5%), followed by the temporoparietal cortex (^{11}C-PIB BP_{ND}: 0.75 ± 0.08; amyloid histology: 13.9% ± 0.7%) and the hippocampus (^{11}C-PIB BP_{ND}: 0.71 ± 0.09; amyloid histology: 9.2% ± 0.9%), and was lowest in the thalamus (^{11}C-PIB BP_{ND}: 0.40 ± 0.07; amyloid histology: 6.6% ± 0.6%). However, ^{11}C-PIB BP_{ND} and amyloid histology linearly correlated ($R^2 = 0.82$, $P < 0.05$) and were significantly higher in transgenic animals ($P < 0.01$). Similarly, microscopic MR imaging allowed quantifying the amyloid load, in addition to the detection of substructures within single amyloid plaques correlating with amyloid deposition density and the measurement of hippocampal atrophy. Finally, we found an inverse relationship between ^{11}C-PIB BP_{ND} and rCBF MR imaging in the voxel-based analysis that was absent in control mice ($slope_{tg}$: −0.11 ± 0.03; $slope_{co}$: 0.004 ± 0.005; $P = 0.014$). **Conclusion:** Our dual-modality imaging approach using ^{11}C-PIB PET/7 T MR imaging and 16.4 T microscopic MR imaging allowed amyloid-load quantification with high sensitivity and high resolution, the identification of substructures within single amyloid plaques, and the quantification of rCBF.

Key Words: PET and MR imaging; microscopic MR imaging; Alzheimer disease; amyloid; rCBF

J Nucl Med 2015; 56:1593–1599
DOI: 10.2967/jnumed.115.159350

One major hallmark of Alzheimer disease (AD) is the prominent deposition of various amyloid species in brain tissue (*1*). Today, a range of transgenic rodent models of AD is available, most of which are models of cerebral β-amyloidosis, either lacking or with only minor additional intraneuronal deposition of neurofibrillary tangles or global neuronal loss as observed in AD patients (*2–8*). However, for studying the quantity or dynamics of amyloid deposition, these animal models are both appropriate and widely used for fundamental research investigations.

Further, noninvasive imaging modalities such as PET, along with specific amyloid tracers (e.g., Pittsburgh compound B [^{11}C-PIB]) or MR imaging allow in vivo studies of the diseased rodent brain. One major reason for the use of MR imaging at a very high spatial resolution (microscopic MR imaging) in brain imaging applications in transgenic AD mouse models is the potential possibility of resolving individual amyloid plaques—possibly even without the use of contrast agents. This approach, however, lacks sensitivity and specificity, as signal voids obtained by T_2- or T_2*-weighted MR imaging may be related to blood vessels oriented in the orthogonal direction relative to the imaging plane or to microhemorrhages (*9*). T_2-weighted acquisitions more precisely reflect the amyloid plaque size, whereas T_2*-weighting yields an iron-sensitive contrast and possibly susceptibility artifacts. However, T_2*-weighting also results in a higher contrast-to-noise-ratio and, thus, enhanced image contrast (*10*). Thus, the combination of T_2*-weighted microscopic MR imaging with a second imaging modality providing high sensitivity and specificity appears logical. Recently, we and others have demonstrated the potential of ^{11}C-PIB PET for selective imaging of amyloid deposits in the brain tissue of transgenic AD mice (*11–13*). Taken together, microscopic MR imaging and ^{11}C-PIB PET potentially provide a powerful combination for the non-invasive quantification and characterization of amyloid deposits at a high spatial resolution and with unmatched sensitivity and specificity.

Further, since the neurophysiology is heavily affected throughout the course of AD (*14,15*), the in vivo assessment of functional parameters such as regional cerebral blood flow (rCBF) is needed

Received Apr. 15, 2015; revision accepted Jul. 21, 2015.
For correspondence or reprints contact: Bernd J. Pichler, Werner Siemens Imaging Center, Department of Preclinical Imaging and Radiopharmacy, University of Tübingen, Röntgenweg 13, 72076 Tübingen, Germany.
E-mail: bernd.pichler@med.uni-tuebingen.de
Published online Aug. 6, 2015.

to validate novel treatment strategies, study the pathophysiology of AD, and for differential clinical diagnosis of AD and other forms of dementia. In the past, the feasibility of arterial spin labeling (ASL) MR imaging for the non-invasive quantification of rCBF in the brain of AD mice has been demonstrated (*16*) and specific ^{11}C-PIB binding has been compared with control animals using voxel-based analysis (*17*). However, to our knowledge, quantitative rCBF has never been compared with ^{11}C-PIB PET on a voxelwise basis in transgenic AD mice.

Thus, our aims were to quantify the amyloid burden in the APP23 mouse brain with in vivo ^{11}C-PIB PET and postmortem microscopic MR imaging at 16.4 T, to correlate rCBF and specific ^{11}C-PIB binding on a voxelwise basis, and to match both approaches to amyloid histology.

MATERIALS AND METHODS

Animals

For all studies, we used female transgenic ($n = 5$) and littermate control ($n = 5$) APP23 mice aged 27.5–30 mo; 4 of the littermate control mice were already included in a previous publication (*13*). APP23 transgenic mice were generated as described previously (*5,13*). All mice were obtained from the Novartis Institutes for BioMedical Research in Basel, Switzerland, and were a kind gift of Dr. Mathias Staufenbiel.

All animals were maintained in our vivarium in isolated ventilated cages on a 12-h day and night cycle at a 22°C room temperature and 50% humidity and with free access to a standard diet and tap water. All animal experiments were performed according to the current guidelines for the care and use of research animals under the German Animal Protection Law. Animal experiments were approved by the local government (Regierungspräsidium Tübingen).

PET Measurements

All PET measurements were performed with a dedicated small-animal PET scanner (Inveon; Siemens Healthcare) with a spatial resolution in the reconstructed images of 1.4 mm (full width at half maximum) at the center of the field of view (*18,19*) and an axial field of view of 12.7 cm. The mice were injected intravenously on the bed with 10.2 ± 0.7 MBq ^{11}C-PIB in 50 μL of 0.9% NaCl with a custom-made catheter (^{11}C-PIB was synthetized according to a previously published method (*20*); details are provided in the Supplemental Methods; available at http://jnm.snmjournals.org). PET emission scans (60 min) were acquired with a coincidence window of 3.4 ns and an energy window of 350–650 keV. Further details are listed in the Supplemental Methods.

MR Imaging Measurements

In vivo MR imaging scans were performed using a horizontal-bore, 7 T small-animal MR tomograph with a maximum gradient strength of 290 mT/m (ClinScan; Bruker BioSpin MR imaging). T_2-weighted images (referred to as tse3DT_2 in the following sections) were used for PET image fusion and region-of-interest definitions using PMOD, version 3.2, image view and fusion tools (PMOD Technologies). Sequence details for all MR imaging sequences are detailed in the Supplemental Methods. rCBF measurements were conducted with single-slice pulsed ASL using a flow-sensitive alternating inversion recovery true fast imaging with steady-state precession approach (*21*). ASL MR imaging data were analyzed using a simplified version of the Bloch equation (Supplemental Methods) and Matlab, version R2009a (The MathWorks), with an in-house-programmed routine.

Ex vivo microscopic MR imaging scans were performed at the Centre for Advanced Imaging, Brisbane, Australia, on a vertical-bore small-animal MR scanner operating at 16.4 T (Avance II; Bruker BioSpin) using a Micro 2.5 gradient system, a 15 mm SAW volume coil, and ParaVision, version 5.1. T_2*-weighted (referred to as highres-3DT_2*) images at high resolution were used for MR imaging–based amyloid plaque quantification.

Data Evaluation

For the evaluation of ^{11}C-PIB PET data, attenuation-corrected scans were analyzed with PMOD, version 3.2, image view and fusion tools. ^{11}C-PIB time–activity curves were analyzed using the Logan graphical analysis method and the cerebellum as reference region yielding non-displaceable binding potentials (BP_{ND}) (*22*).

Amyloid quantification was estimated from both microscopic MR imaging and amyloid histology. As the exact spatial matching of microscopic MR imaging and histologic slides is difficult, we used a statistical approach to estimate the total amyloid burden of each region. Every third slice of the microscopic MR imaging scans, corresponding to every 12th–14th slice of the paraffin-embedded brains, was used to quantify the amyloid burden, with a total of 3 slice groups for microscopic MR imaging and amyloid histology. Further details, along with the histologic procedures and a description of the data analysis method used for the voxel-based correlation of ^{11}C-PIB PET and ASL MR imaging, are listed in the Supplemental Methods.

Statistics

Differences in ^{11}C-PIB BP_{ND} between transgenic and littermate control mice were compared using the Mann–Whitney *U* test, and *P* values of less than 0.05 were considered statistically significant. ^{11}C-PIB PET and ASL MR imaging voxelwise correlation quadrant assignments are displayed as median with the respective interquartile range. Testing of homoscedasticity between comparison groups was performed using the Brown–Forsythe test and the Origin, version 8.0, Pro software package (OriginLab). It was further ensured that the data included in the analyses met all assumptions of the used statistical tests before statistical testing and data interpretation were conducted. All values are represented as the average ± SE of the mean (SEM), unless stated otherwise. All regression analyses and statistical tests were performed with the Origin, version 8.0, Pro software package and the JMP, version 10.0.2, software package (SAS Institute GmbH). No animals were excluded from the data analysis.

RESULTS

Quantification of the Amyloid Burden with ^{11}C-PIB PET

First, we analyzed specific ^{11}C-PIB binding in transgenic and littermate control APP23 mice. Figure 1A shows an example of ^{11}C-PIB PET/tse3DT_2 MR image fusion. The highest BP_{ND} in comparison to control animals were observed in the frontal cortex of APP23 mice (transgenic: 0.93 ± 0.08; control: 0.11 ± 0.02; $n = 5$, $P < 0.01$). Comparable BP_{ND} were found in the temporoparietal cortex and the hippocampus (transgenic: 0.75 ± 0.08 in temporoparietal cortex and 0.71 ± 0.09 in hippocampus; control: 0.10 ± 0.01 in temporoparietal cortex and 0.03 ± 0.01 in hippocampus; $n = 5$, $P < 0.01$). The lowest ^{11}C-PIB BP_{ND} were calculated for the thalamus (transgenic: 0.40 ± 0.07; control: 0.02 ± 0.01; $n = 5$, $P < 0.01$; all ^{11}C-PIB BP_{ND} are illustrated in Fig. 1B). Further, we assessed the amyloid load histologically in the same animals after the last imaging experiment was conducted for 16.4 T MR imaging. Figure 1B shows the quantified amyloid burden (expressed as percentage of the volume of interest, covered with deposited amyloid) in the brain regions that were examined by dedicated PET and MR imaging. Again, the highest amyloid load was in the frontal cortex (transgenic: 15.1% ± 1.5%; control: 0.24% ± 0.03%; $n = 5$, $P < 0.01$), followed by the temporoparietal cortex (transgenic: 13.9% ± 0.7%; control: 0.16% ± 0.03%; $n = 5$, $P < 0.01$), the hippocampus (transgenic: 9.2% ± 0.9%; control: 0.25% ± 0.08%; $n = 5$, $P < 0.01$) and the thalamus (transgenic: 6.6% ± 0.6%; control: 0.11% ± 0.04%; $n = 5$,

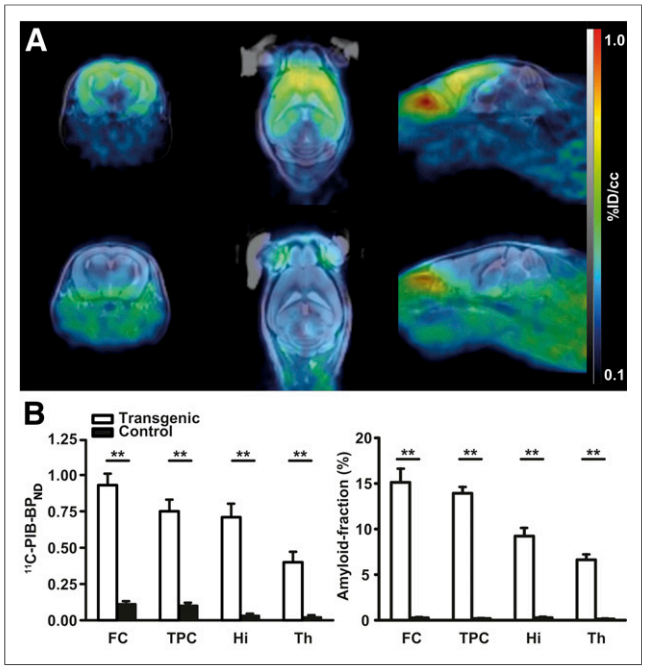

FIGURE 1. Quantification of amyloid burden with ^{11}C-PIB PET and amyloid histology. (A) Transversal, horizontal, and sagittal views of fused ^{11}C-PIB PET/tse3DT$_2$ MR imaging at 7 T of 30-mo-old transgenic APP23 mouse (upper panel) and of age-matched control mouse (lower panel). Note specific ^{11}C-PIB binding in amyloid-affected brain regions of transgenic animal (frontal cortex, hippocampus, temporoparietal cortex, thalamus) in contrast to cerebellum, which is amyloid-unaffected. (B) Quantification of ^{11}C-PIB BP$_{ND}$ in transgenic and control mice reveals significantly higher binding in transgenic mice ($n = 5$) and matches amyloid load assessed by amyloid histology ($n = 5$). $^{**}P < 0.01$. FC = frontal cortex; TPC = temporoparietal cortex; Hi = hippocampus ; Th = thalamus.

$P < 0.01$, 2-sided unpaired t test). ^{11}C-PIB BP$_{ND}$ and amyloid histology were linearly correlated (Supplemental Fig. 1); however, the comparable ^{11}C-PIB BP$_{ND}$ of the temporoparietal cortex and the hippocampus could not be reproduced in the amyloid histology (Fig. 1B). This is most probably attributable to partial-volume effects.

Correlation of ^{11}C-PIB PET, High-Resolution Gre3DT$_2$* Microscopic MR Imaging at 16.4 T, and Amyloid Histology

After dedicated in vivo PET and MR imaging examinations, the mice were euthanized and their brains harvested and sent to our Australian collaboration partners. There, the brains were prepared for ex vivo high-resolution microscopic MR imaging at 16.4 T. Figures 2A and 2B show an example of dedicated in vivo ^{11}C-PIB PET and MR imaging at 7 T, Figure 2C shows the corresponding ex vivo microscopic MR imaging at 16.4 T in the frontal cortex of the same animal (bregma: 0.14 mm), and Figure 2D shows the correlation of ^{11}C-PIB BP$_{ND}$ and the microscopic MR imaging–derived amyloid load for this transgenic mouse ($R^2 = 0.98$). Similar to the histology, we chose to express the amyloid load as percentage of the microscopic MR imaging volume of interest that was covered with deposited amyloid.

Figure 3A illustrates a microscopic MR imaging section of the same brain as shown in Figure 2C at the level of the temporoparietal cortex (bregma: −1.94 mm). The amyloid deposition pattern estimated from microscopic MR imaging (Fig. 3A) corresponds well with the respective amyloid histology (Fig. 3B) in the temporoparietal cortex, especially in the piriform cortex (Fig. 3D). The amyloid deposition in the hippocampus and the thalamus is not perfectly matched (Figs. 3A and 3B), which is most likely attributable to deviations between the 3-dimensional orientation of the sectional planes of microscopic MR imaging and amyloid histology. At a higher magnification, substructures within amyloid deposits in the T$_2$*-weighted microscopic MR imaging and the amyloid histology can be clearly identified (Fig. 3D). The observed substructures, characterized by lower signal intensities in the T$_2$*-weighted microscopic MR imaging, correspond to dense-cored amyloid within senile plaques (Fig. 3D; achievable contrast-to-noise ratio described in the Supplemental Results). Figure 3C provides an example of T$_2$*-weighted microscopic MR imaging of an age-matched littermate control mouse. Areas with lower signal intensities can be clearly identified either as blood vessels in the temporoparietal cortex (parallel to the imaging plane) or as blood vessels transverse to the imaging plane (caudal to the dentate gyrus or to axon bundles such as the mammillothalamic tract or the perifornical nucleus) (arrowheads in Fig. 3C indicate the mentioned structures). However, T$_2$* signal voids comparable to those observed in transgenic APP23 mice were located neither in the frontal cortex, the temporoparietal cortex, the hippocampus, nor the thalamus, and hence, T$_2$*-weighted microscopic MR imaging enables a clear separation of the control from the transgenic APP23 mouse brain (Supplemental Results and Supplemental Fig. 3).

Voxel-Based Correlation of ^{11}C-PIB PET and ASL MR Imaging at 7 T

After the ^{11}C-PIB PET acquisitions, we investigated the same animals with ASL MR imaging at 7 T to quantify physiologic

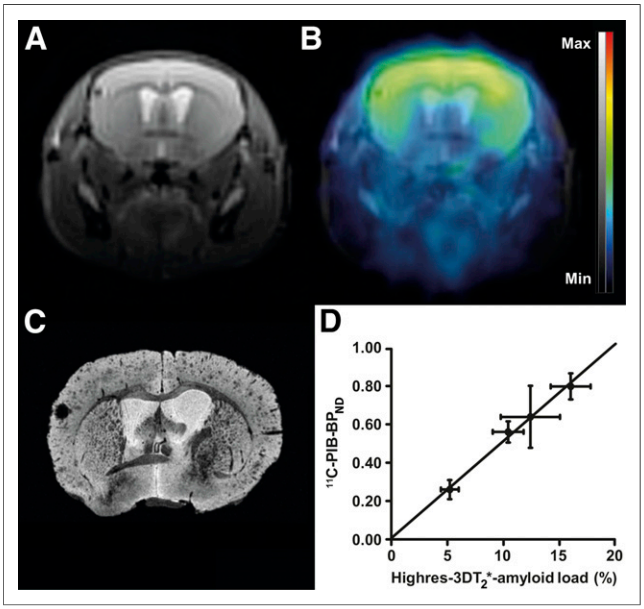

FIGURE 2. Correlation of ^{11}C-PIB PET and T$_2$*-weighted microscopic MR imaging at 16.4 T. (A–C) Example of tse3DT$_2$ MR imaging at 7 T (A), corresponding dedicated ^{11}C-PIB PET and MR imaging overlay (B), and respective postmortem T$_2$*-weighted imaging (C) at 16.4 T of same 30-mo-old transgenic APP23 mouse as shown in Figure 1. (D) ^{11}C-PIB BP$_{ND}$ and microscopic MR imaging amyloid fractions calculated from T$_2$*-weighted imaging at 16.4 T were correlated linearly ($R^2 = 0.98$, Pearson correlation coefficient; $P = 0.99$; data are shown for animal presented in A–C and refer to ^{11}C-PIB BP$_{ND}$ ± SE of Logan fitting routine and percentage of T$_2$*-weighted amyloid-positive fraction of thalamus, hippocampus, temporoparietal cortex, and frontal cortex). Highres-3DT$_2$* = T$_2$*-weighted.

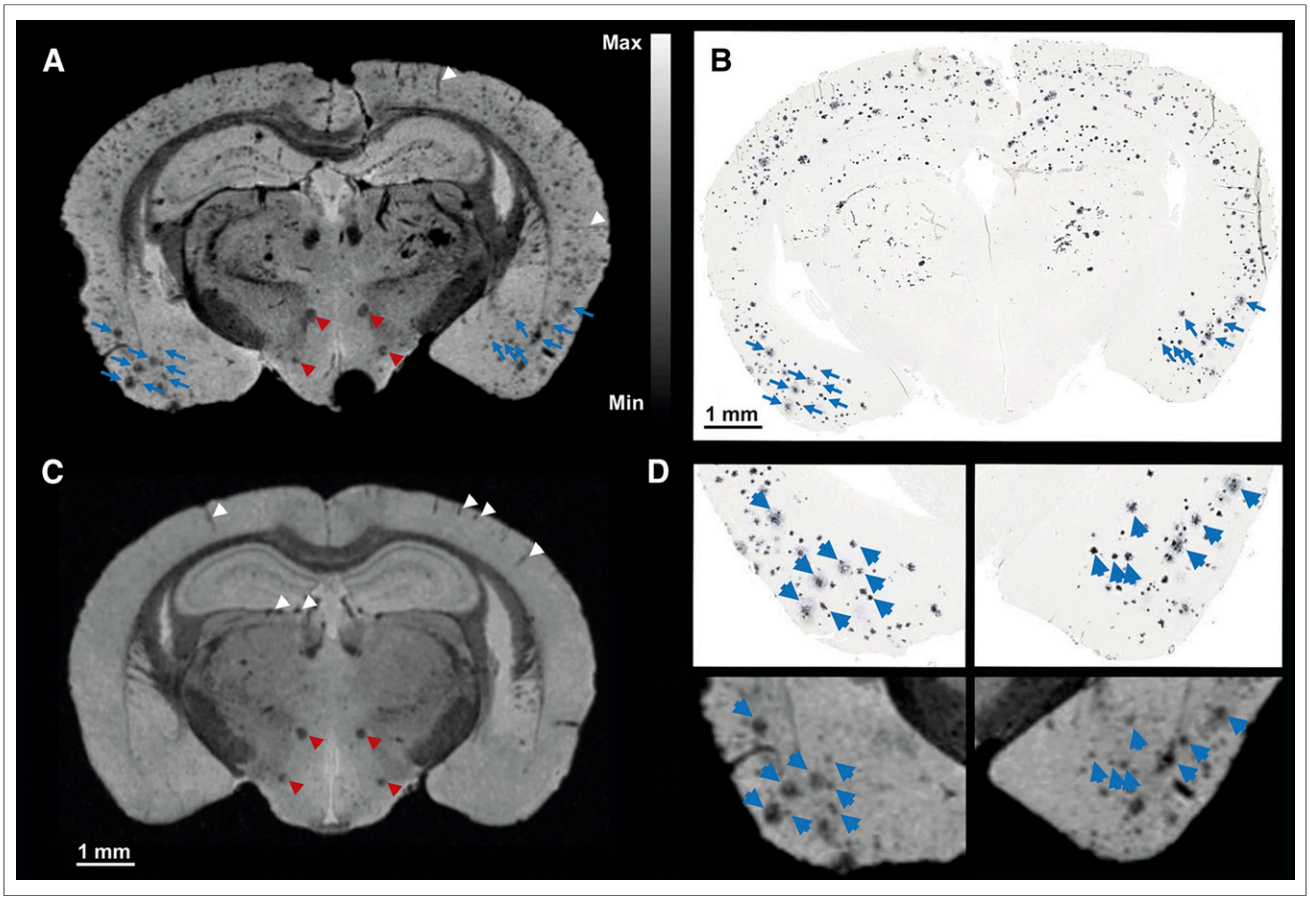

FIGURE 3. Correlation of T_2*-weighted microscopic MR imaging at 16.4 T and amyloid histology. T_2*-weighted image (A) at 16.4 T of 30-mo-old transgenic APP23 mouse and corresponding amyloid histology (B), with matching amyloid plaques are indicated by blue arrowheads. (C) T_2*-weighted image at 16.4 T of littermate control APP23 mouse. Only rare hypointensities are present in temporoparietal cortex corresponding to blood vessels parallel to imaging plane or in hippocampus orthogonal to imaging plane (indicated by white arrowheads). Mammillothalamic tract and perifornical nucleus are indicated by red arrowheads. (D) Higher magnification of A and B allows identification of substructures within single amyloid plaques that are related to density of amyloid deposition (blue arrowheads).

alterations accompanying amyloid deposition (the ^{11}C-PIB PET and ASL MR imaging results of 4 control mice were already included in a previous study (*13*); however, here we used a novel, voxel-based data analysis method). Methodologic details are provided in the Supplemental Methods and Supplemental Figure 5.

Clusters for all analyzed regions of interest are displayed for one transgenic and one control mouse in Figure 4B; the respective ASL MR imaging scans are provided in Supplemental Figure 4. We chose to introduce 2 gates in the respective ^{11}C-PIB/rCBF scatterplots to separate 4 possible voxel populations characterized by high ^{11}C-PIB/low rCBF (quadrant 1), high ^{11}C-PIB/normal rCBF (quadrant 2), low ^{11}C-PIB/low rCBF (quadrant 3), or low ^{11}C-PIB/normal rCBF (quadrant 4) (Fig. 4B). The cutoff values for subsequent gating were chosen at a 95.45% probability population threshold directly from the gaussian distributions of the ^{11}C-PIB PET and ASL MR imaging voxel values of littermate control mice (mean ± 2 SDs of the gaussian distribution, corresponding to 95.45% of all values; Supplemental Table 1). As expected, the majority of the ^{11}C-PIB/rCBF voxels in transgenic APP23 mice on a group level (n = 5 mice, 3,903 voxels) were in quadrant 1 (26.9%; range, 16.3%–46.8%) and quadrant 2 (62.7%; range, 51.4%–77.0%), whereas 0.0% (range, 0.0%–0.4%) were assigned to quadrant 3 and 6.7% (range, 0.0%–18.2%) to quadrant 4 (Fig. 4D shows the quadrant distribution for 1 transgenic mouse). The results in control animals were diametrically opposed (group level, n = 5 mice, 3,901 voxels): 0.0% (range, 0.0%–0.0%) were in quadrant 1, 0.0% (range, 0.0%–40.1%) in quadrant 2, 0.6% (range, 0.0%–1.9%) in quadrant 3, and 98.5% (range, 59.8%–99.9%) in quadrant 4 (Fig. 4D shows the quadrant distribution for 1 control mouse). Further, we applied a linear fit to the voxel-based scatterplots of all animals and clearly observed an inverse correlation of ^{11}C-PIB binding and rCBF in transgenic mice on a group level (slope: −0.107 ± 0.030, n = 5 mice, inset Fig. 4B), whereas there was no correlation in control mice on a group level (slope: 0.004 ± 0.005, n = 5 mice, inset Fig. 4B, linear fits for 2 mice in Fig. 4B). Taken together, the 2 presented analysis approaches allowed a clear separation of transgenic APP23 from littermate control mice.

DISCUSSION

Because new amyloid-targeted treatment concepts are on the horizon, more refined PET and MR imaging protocols and data analysis methods are required for clinical differential diagnosis and to fully understand treatment effects and efficacy. The major motivation behind the use of ^{11}C-PIB PET in both clinical and basic research settings of AD is to quantify amyloid load with high

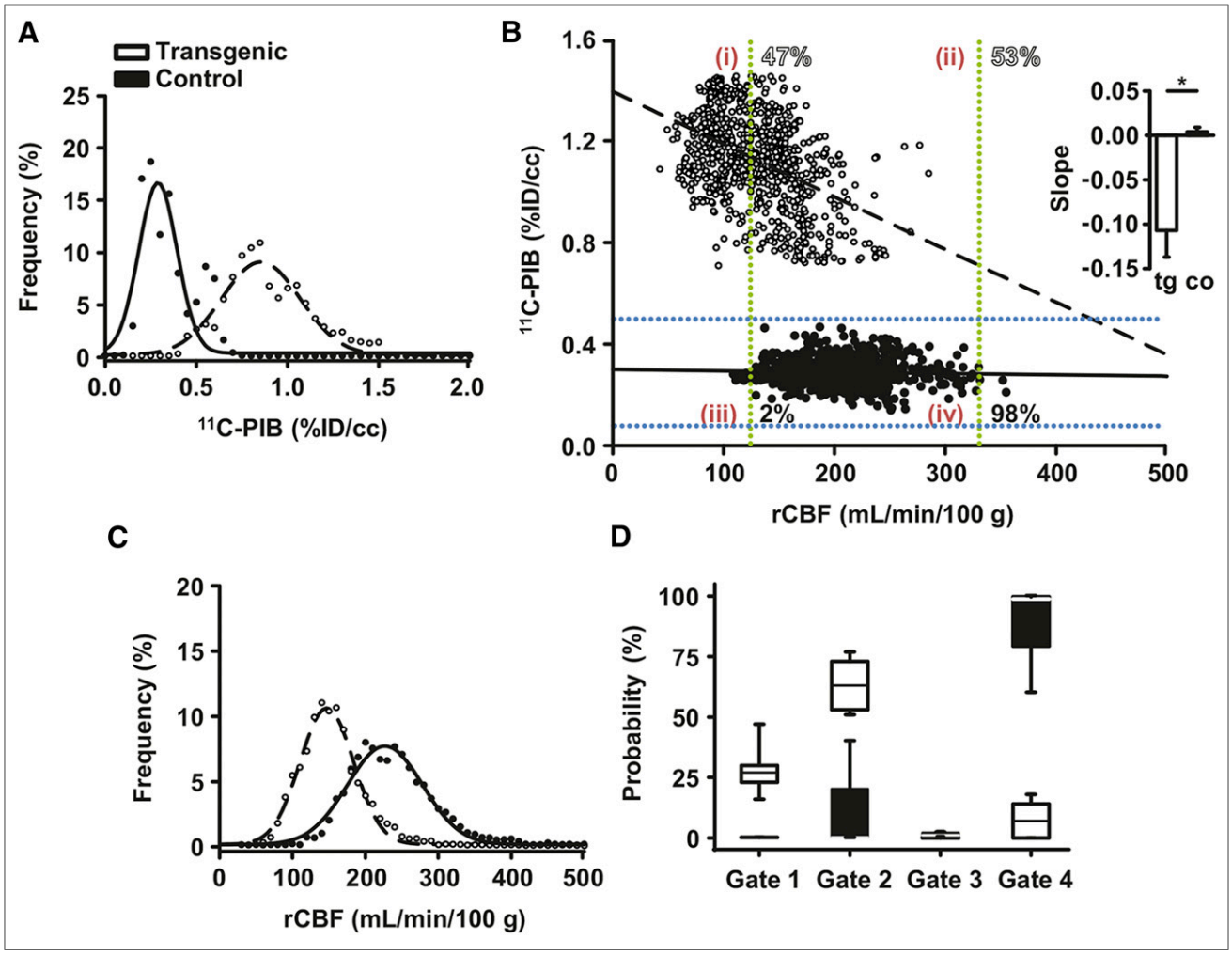

FIGURE 4. Voxel-based correlation of ^{11}C-PIB PET and ASL MR imaging at 7 T. (A and C) Frequency distribution and gaussian fits of ^{11}C-PIB (A) and of rCBF values (C). (B) Example of 2-dimensional voxelwise correlation of 30-mo-old transgenic and littermate control APP23 mouse. Mean ± 2 SD thresholds calculated from A and C are indicated by dashed lines (blue: ^{11}C-PIB thresholds; green: ASL thresholds). This allows assignment of 2-dimensional voxelwise datasets to 4 described gates (indicated by red numbers), gate assignments as percentage for both animals are shown in open numbers (transgenic) and solid numbers (control). (Inset: linear fits to voxelwise correlation plots revealed inverse correlation of ^{11}C-PIB and rCBF in transgenic APP23 mice; littermate controls displayed no such correlation ($n = 5$, $P < 0.05$)). (D) Two-dimensional voxel-value probability distribution of all transgenic and control APP23 mice (shown is voxel distribution in 4 gates as percentage).

sensitivity, whereas the driving force behind the use of microscopic MR imaging is to measure amyloidosis at the spatial resolution of single amyloid plaques—ideally without the need for externally administered contrast agents. Recently, it was proven that ^{11}C-PIB binding does not necessarily serve as a surrogate marker for disease severity in AD (*8*) but rather as a tool for the dichotomous division of the examined subjects. Thus, adding measurement protocols such as ASL MR imaging is crucial to understand the physiologic alterations accompanying amyloid deposition.

So far, only few reports have demonstrated the feasibility of ^{11}C-PIB PET in fundamental research applications using small-animal models of cerebral β-amyloidosis, although this method is gathering momentum (*11,12,17,23*). On the other hand, other groups have shown the feasibility of using high-resolution microscopic MR imaging to detect single amyloid plaques (*1,9,24–26*). This approach, however, lacks sensitivity and specificity as signal voids originating from T_2- or T_2*-weighted MR imaging may be related to blood vessels oriented in the orthogonal direction relative to the imaging plane or to microhemorrhages. Although the combination of microscopic MR imaging with an imaging protocol providing high sensitivity and specificity appears logical, to our knowledge this has not been previously reported. We demonstrate for the first time the excellent correlation of ^{11}C-PIB PET, T_2*-weighted microscopic MR imaging, and amyloid histology.

Recent studies exclusively investigated different APPPS1 mouse models and Tg2576 mice (*1,9,24–26*), whereas we used the APP23 mouse model, harboring much larger parenchymal amyloid deposits that are mostly dense-cored and congophilic. This approach also enabled, for the first time, the detection of substructures within amyloid deposits—correlating with the histologic phenotypes and density of the amyloid deposition within single plaques. It has been hypothesized that the inherent contrast of parenchymal β-amyloid deposits in either T_2- or

T_2*-weighted microscopic MR imaging is caused either by paramagnetic iron accumulation within the core of the amyloid plaque or by the dense packing of highly ordered amyloid fibrils, finally forming a congophilic dense-cored deposit. Wengenack et al. reported that the fast decay of transverse magnetization (T_2*) is not solely attributed to the presence of iron within the amyloid plaques in the cortex and hippocampus in APPPS1 double transgenic mice (*27*). This notion was further supported by Nabuurs et al., as only fibrillar amyloid plaques rather than diffuse plaques induced significant changes in either T_2 or T_2* values and the loss of transverse magnetization was not necessarily correlated with the presence of iron within amyloid deposits (*28*). We now provide further evidence that the density of the amyloid deposition is a key factor for fast transverse magnetization decay, as T_2* signal intensity is inversely correlated with amyloid deposition density within single amyloid plaques. One major advantage of microscopic MR imaging is that it is fast, efficient, and less labor-intensive than histologic examinations. In addition, microscopic MR imaging allows fully 3-dimensional volume quantification—in sharp contrast to histology. The cross correlation of microscopic MR imaging and histologic datasets remains difficult as there are always uncertainties in the coregistration that can be caused by noniso-tropic deformations of the brain tissue by dehydration (*24*). The strength of a combined PET and MR imaging approach is the specific identification of amyloid deposits by amyloid PET, while at the same time, high-resolution microscopic MR imaging renders the identification of individual plaques feasible although it does not solve the problem of misidentification of non-APP deposits (*29,30*). Further details regarding the limitations and benefits of microscopic MR imaging and PET are provided in the Supplemental Discussion.

We also demonstrate that ^{11}C-PIB binding and rCBF were inversely correlated on a voxelwise basis in 27.5- to 30-mo-old APP23 mice, whereas control animals displayed no such correlation (in accordance with previous findings by our group). Our gaussian-based gating approach for a voxel-based analysis and the separation of specific clusters could be useful in any multiparametric imaging application. The respective clusters could be back-projected onto the original imaging data to aid the identification of diseased tissue. In the future, we plan to compare the presented data with different supervised or unsupervised support vector machine learning approaches.

CONCLUSION

Microscopic MR imaging and ^{11}C-PIB PET provide a powerful combination for the quantification of amyloid deposits at high spatial resolution and with unmatched sensitivity and specificity. The combination of amyloid-targeted imaging approaches with examinations of the accompanying physiology in the AD brain potentially aids disease staging and the evaluation of new treatment strategies, enabling morphologic and functional classification of the underlying mechanism of action.

DISCLOSURE

The costs of publication of this article were defrayed in part by the payment of page charges. Therefore, and solely to indicate this fact, this article is hereby marked "advertisement" in accordance with 18 USC section 1734. This work was funded by BMBF grant 01 Gi 0705 and DFG grant PI 771/1-1. Prof. Pichler receives grant or research support from AstraZeneca, Bayer Healthcare, Boehringer-Ingelheim, Bruker, Oncodesign, Merck, and Siemens; none of the grants are directly related to this work. Prof. Galloway receives research support from Siemens; however, it is not related to this work. No other potential conflict of interest relevant to this article was reported.

ACKNOWLEDGMENTS

We thank Maren Harant for excellent technical assistance during in vivo experiments; Anke Stahlschmidt, Walter Ehrlichmann, and Gerald Reischl for providing ^{11}C-PIB; Mathias Staufenbiel for kindly providing transgenic and littermate control APP23 mice; and the Queensland NMR Network and the Queensland node of the National Imaging Facility for technical support.

REFERENCES

1. Härtig W, Goldhammer S, Bauer U, et al. Concomitant detection of beta-amyloid peptides with N-terminal truncation and different C-terminal endings in cortical plaques from cases with Alzheimer's disease, senile monkeys and triple transgenic mice. *J Chem Neuroanat.* 2010;40:82–92.
2. Hsiao K, Chapman P, Nilsen S, et al. Correlative memory deficits, Abeta elevation, and amyloid plaques in transgenic mice. *Science.* 1996;274:99–102.
3. Radde R, Bolmont T, Kaeser SA, et al. Abeta42-driven cerebral amyloidosis in transgenic mice reveals early and robust pathology. *EMBO Rep.* 2006;7:940–946.
4. Radde R, Duma C, Goedert M, Jucker M. The value of incomplete mouse models of Alzheimer's disease. *Eur J Nucl Med Mol Imaging.* 2008;35(suppl 1):S70–S74.
5. Sturchler-Pierrat C, Abramowski D, Duke M, et al. Two amyloid precursor protein transgenic mouse models with Alzheimer disease-like pathology. *Proc Natl Acad Sci USA.* 1997;94:13287–13292.
6. Calhoun ME, Wiederhold KH, Abramowski D, et al. Neuron loss in APP transgenic mice. *Nature.* 1998;395:755–756.
7. Rupp NJ, Wegenast-Braun BM, Radde R, Calhoun ME, Jucker M. Early onset amyloid lesions lead to severe neuritic abnormalities and local, but not global neuron loss in APPPS1 transgenic mice. *Neurobiol Aging.* 2011;32:2324 e2321–2326.
8. Weiner MW, Veitch DP, Aisen PS, et al. The Alzheimer's Disease Neuroimaging Initiative: a review of papers published since its inception. *Alzheimers Dement.* 2012;8(suppl):S1–S68.
9. Poduslo JF, Wengenack TM, Curran GL, et al. Molecular targeting of Alzheimer's amyloid plaques for contrast-enhanced magnetic resonance imaging. *Neurobiol Dis.* 2002;11:315–329.
10. Jack CR Jr, Garwood M, Wengenack TM, et al. In vivo visualization of Alzheimer's amyloid plaques by magnetic resonance imaging in transgenic mice without a contrast agent. *Magn Reson Med.* 2004;52:1263–1271.
11. Maeda J, Ji B, Irie T, et al. Longitudinal, quantitative assessment of amyloid, neuroinflammation, and anti-amyloid treatment in a living mouse model of Alzheimer's disease enabled by positron emission tomography. *J Neurosci.* 2007;27:10957–10968.
12. Manook A, Yousefi BH, Willuweit A, et al. Small-animal PET imaging of amyloid-beta plaques with [^{11}C]PiB and its multi-modal validation in an APP/PS1 mouse model of Alzheimer's disease. *PLoS One.* 2012;7:e31310.
13. Maier FC, Wehrl HF, Schmid AM, et al. Longitudinal PET-MRI reveals β-amyloid deposition and rCBF dynamics and connects vascular amyloidosis to quantitative loss of perfusion. *Nat Med.* 2014;20:1485–1492.
14. Bateman RJ, Xiong C, Benzinger TL, et al. Clinical and biomarker changes in dominantly inherited Alzheimer's disease. *N Engl J Med.* 2012;367:795–804.
15. Jack CR Jr, Knopman DS, Jagust WJ, et al. Hypothetical model of dynamic biomarkers of the Alzheimer's pathological cascade. *Lancet Neurol.* 2010;9:119–128.
16. Weidensteiner C, Metzger F, Bruns A, Bohrmann B, Kuennecke B, von Kienlin M. Cortical hypoperfusion in the B6.PS2APP mouse model for Alzheimer's disease: comprehensive phenotyping of vascular and tissular parameters by MRI. *Magn Reson Med.* 2009;62:35–45.
17. von Reutern B, Grunecker B, Yousefi BH, Henriksen G, Czisch M, Drzezga A. Voxel-based analysis of amyloid-burden measured with [^{11}C]PiB PET in a double transgenic mouse model of Alzheimer's disease. *Mol Imaging Biol.* 2013;15:576–584.

18. Bao Q, Newport D, Chen M, Stout DB, Chatziioannou AF. Performance evaluation of the Inveon dedicated PET preclinical tomograph based on the NEMA NU-4 standards. *J Nucl Med.* 2009;50:401–408.
19. Mannheim JG, Judenhofer MS, Schmid A, et al. Quantification accuracy and partial volume effect in dependence of the attenuation correction of a state-of-the-art small animal PET scanner. *Phys Med Biol.* 2012;57:3981–3993.
20. Solbach C, Uebele M, Reischl G, Machulla HJ. Efficient radiosynthesis of carbon-11 labelled uncharged thioflavin T derivatives using [^{11}C]methyl triflate for beta-amyloid imaging in Alzheimer's disease with PET. *Appl Radiat Isot.* 2005;62:591–595.
21. Fenchel M, Martirosian P, Langanke J, et al. Perfusion MR imaging with FAIR true FISP spin labeling in patients with and without renal artery stenosis: initial experience. *Radiology.* 2006;238:1013–1021.
22. Logan J, Fowler JS, Volkow ND, Wang GJ, Ding YS, Alexoff DL. Distribution volume ratios without blood sampling from graphical analysis of PET data. *J Cereb Blood Flow Metab.* 1996;16:834–840.
23. Snellman A, Lopez-Picon FR, Rokka J, et al. Longitudinal amyloid imaging in mouse brain with ^{11}C-PIB: comparison of APP23, Tg2576, and APPswe-PS1dE9 mouse models of Alzheimer disease. *J Nucl Med.* 2013;54:1434–1441.
24. Meadowcroft MD, Connor JR, Smith MB, Yang QX. MRI and histological analysis of beta-amyloid plaques in both human Alzheimer's disease and APP/PS1 transgenic mice. *J Magn Reson Imaging.* 2009;29:997–1007.
25. Wadghiri YZ, Sigurdsson EM, Sadowski M, et al. Detection of Alzheimer's amyloid in transgenic mice using magnetic resonance microimaging. *Magn Reson Med.* 2003;50:293–302.
26. Yang J, Wadghiri YZ, Hoang DM, et al. Detection of amyloid plaques targeted by USPIO-Abeta1-42 in Alzheimer's disease transgenic mice using magnetic resonance microimaging. *Neuroimage.* 2011;55:1600–1609.
27. Wengenack TM, Reyes DA, Curran GL, et al. Regional differences in MRI detection of amyloid plaques in AD transgenic mouse brain. *Neuroimage.* 2011;54:113–122.
28. Nabuurs RJ, Natte R, de Ronde FM, et al. MR microscopy of human amyloid-beta deposits: characterization of parenchymal amyloid, diffuse plaques, and vascular amyloid. *J Alzheimers Dis.* 2013;34:1037–1049.
29. Ghiso J, Revesz T, Holton J, et al. Chromosome 13 dementia syndromes as models of neurodegeneration. *Amyloid.* 2001;8:277–284.
30. Vidal R, Frangione B, Rostagno A, et al. A stop-codon mutation in the BRI gene associated with familial British dementia. *Nature.* 1999;399:776–781.